AGU PUBLICATIONS

Geophysical Research Letters

RESEARCH LETTER
10.1002/2015GL066409

Key Points:
- Daily snapshots of TIL strength
- Synoptic-scale behavior of the TIL and shear/curl contributions to relative vorticity
- TIL within ridges in midlatitude winter is stronger than polar summer TIL

Supporting Information:
- Figures S1–S6

Correspondence to:
R. Pilch Kedzierski,
rpilch@geomar.de

Citation:
Pilch Kedzierski, R., K. Matthes, and K. Bumke (2015), Synoptic-scale behavior of the extratropical tropopause inversion layer, *Geophys. Res. Lett.*, *42*, 10,018–10,026, doi:10.1002/2015GL066409.

Received 1 OCT 2015
Accepted 29 OCT 2015
Accepted article online 2 NOV 2015
Published online 19 NOV 2015

Synoptic-scale behavior of the extratropical tropopause inversion layer

Robin Pilch Kedzierski[1], Katja Matthes[1,2], and Karl Bumke[1]

[1] Marine Meteorology Department, GEOMAR Helmholtz Centre for Ocean Research Kiel, Kiel, Germany, [2] Faculty of Mathematics and Natural Sciences, Christian-Albrechts-Universität zu Kiel, Kiel, Germany

Abstract High-resolution GPS radio occultation temperature profiles from the COSMIC satellite mission (2007–2013) are used to obtain daily snapshots of the strength of the extratropical tropopause inversion layer (TIL). Its horizontal structure and day-to-day variability are linked to the synoptic situation at near-tropopause level. The strength of the TIL in cyclonic as well as anticyclonic conditions is investigated by separating relative vorticity into curl and shear terms. The analysis shows that the TIL has high zonal variability, and its strength is instantaneously adjusted to the synoptic situation at near-tropopause level. Our key finding is that the TIL within midlatitude ridges in winter is as strong as or stronger than the TIL in polar summer. The strongest TIL in anticyclonic conditions is related to the shear term, while the weaker TIL in cyclonic conditions is enhanced by the curl term.

1. Introduction

The extratropical tropopause inversion layer (TIL) is characterized by enhanced static stability and a strong temperature inversion in a thin layer of about 1 km depth right above the extratropical tropopause. The TIL was discovered via tropopause-based averaging [*Birner et al.*, 2002] and is a ubiquitous global phenomenon from high vertically resolved radiosonde observations [*Birner*, 2006] and satellite GPS radio occultation (GPS-RO) temperature profiles [*Grise et al.*, 2010].

The TIL receives increasing attention because its enhanced stability has implications for the vertical propagation of Rossby and small-scale gravity waves. Since a number of refraction indexes and wave theory approximations make use of static stability in their formulas, higher static stability would act to inhibit vertical wave propagation [see *Birner*, 2006, and references therein].

TIL seasonality, vertical structure, and strength are strongly correlated with observed gradients of stratospheric and tropospheric trace gases from aircraft [*Kunz et al.*, 2009; *Schmidt et al.*, 2010] and satellite measurements [*Hegglin et al.*, 2009]. Therefore, it is argued that the TIL plays an important role in stratosphere-troposphere exchange (STE), which determines stratospheric chemical composition and affects the radiation budget for surface climate. The relation is as follows: higher static stability inhibits vertical motion and correlates with sharper trace gas gradient which in turn inhibits STE.

Climatological studies have shown that the TIL is strongest in polar summer and also has a relative maximum in midlatitude winter [*Birner*, 2006; *Randel et al.*, 2007; *Randel and Wu*, 2010; *Grise et al.*, 2010]. The TIL is enhanced under anticyclonic conditions based on GPS-RO observations [*Randel et al.*, 2007; *Randel and Wu*, 2010]. Given that the temperature decreases with height up to the tropopause where the gradient is reversed, a dipole of cooling below the tropopause and warming above the tropopause is needed for the enhancement of the gradient right above the tropopause. Several hypotheses have been proposed about what mechanisms can produce this dipole and thus form and maintain the TIL:

1. Radiative effects: These involve longwave water vapor cooling below the tropopause and shortwave ozone warming above the tropopause due to their decreasing (increasing) concentration with height. This mechanism was first proposed by *Randel et al.* [2007]. Later the role of water vapor was found to be dominant [*Hegglin et al.*, 2009; *Kunz et al.*, 2009; *Randel and Wu*, 2010]. However, modeling studies by *Birner* [2010] and *Miyazaki et al.* [2010a] suggest that radiative effects are only important during summer.
2. Dynamics: The dipole consists of dynamical heating above the tropopause driven by the downwelling branch of the large-scale stratospheric residual circulation and cooling below the tropopause due to

tropopause lifting by upper tropospheric eddies. *Birner* [2010] showed a TIL formation by including the dynamical effects of stratospheric residual circulation in a chemistry climate model, and a number of idealized modeling studies pointed to the importance of synoptic-scale dynamics alone: baroclinic waves and their embedded cyclones and anticyclones [*Wirth*, 2003, 2004; *Wirth and Szabo*, 2007; *Son and Polvani*, 2007] and specially baroclinic wave breaking events [*Erler and Wirth*, 2011] in the formation and enhancement of the TIL. Yet this dipole only explains the magnitude of the TIL found at midlatitudes, and the only observational studies making a direct link between TIL variability and dynamics are *Randel et al.* [2007] and *Randel and Wu* [2010] on the relationship between the TIL and near-tropopause cyclonic-anticyclonic relative vorticity. At small scales, a baroclinic life cycle experiment by *Kunkel et al.* [2014] showed transient enhancement of the TIL in the presence of gravity waves, which could persistently enhance/maintain the TIL via wave-mean flow interaction.

The current state of research suggests that the TIL, though a global phenomenon, has different formation processes which depend on latitude and season. The relative contribution of each was studied in a high-resolution model [*Miyazaki et al.*, 2010a, 2010b] and supports the idea that radiative effects are of importance only in polar summer while dynamics dominate otherwise.

The main goals of our study are to provide a first detailed observational picture of the TIL's real-time behavior and to gain insight into the role of synoptic-scale dynamics on the TIL formation and maintenance. We will contrast the polar summer TIL to the TIL found within baroclinic waves in winter. The high number of temperature profiles from GPS-RO observations from the COSMIC satellite mission [*Anthes et al.*, 2008] allows to derive daily snapshots of TIL properties at a sufficient horizontal resolution to be compared to the synoptic situation at near-tropopause level from ERA-Interim reanalysis [*Dee et al.*, 2011]. Also, we investigate the relationship between the TIL and cyclonic versus anticyclonic conditions by splitting relative vorticity into curl and shear terms. Shear represents pure horizontal wind gradient as from balanced adiabatic dynamics. Curl, an air parcel's spin, becomes important during the high-amplitude and breaking stages of a baroclinic wave [*Bell and Keyser*, 1993], and high values indicate flow imbalance [*Plougonven and Zhang*, 2014; *Kunkel et al.*, 2014]. Our interest is which term and its associated flow type enhances the TIL at different relative vorticity conditions.

In sections 2.1 and 2.2 we will explain, respectively, the methods to obtain TIL daily snapshots and to split relative vorticity into curl and shear terms. In section 3 the synoptic-scale behavior of the TIL will be analyzed; section 4 will discuss the relative contributions of curl and shear on the TIL relationship with cyclonic-anticyclonic relative vorticity; and section 5 will discuss and summarize the main findings.

2. Data and Methods

To derive TIL properties, we use temperature profiles from GPS-RO observations (COSMIC satellite mission [*Anthes et al.*, 2008]). The high vertical resolution of the GPS-RO temperature profiles (100 m spacing from the ground up to 40 km altitude) is comparable to that of high-resolution radiosondes, with the advantage of having weather independency and global coverage at a rate of ~2000 profiles per day. The wet temperature profiles we use (the "wetPrf" product) include the water vapor effect when retrieving temperature from the refractivity measured by the satellites, based on a 1D variational analysis using European Centre for Medium-Range Weather Forecasts (ECMWF) data. Higher concentrations or gradients of water vapor near the tropopause are not an error source this way. The "wetPrf" and dry temperature "atmPrf" profiles agree extremely well in a validation study by *Das and Pan* [2014], with absolute zero difference above the 200 hPa level. Less than 1% of the profiles is rejected by a preliminary quality control. Profiles with temperatures $>150°C$ or $<-150°C$ and those where the tropopause cannot be detected are not used to avoid unrealistic temperature gradients and/or TIL location.

The tropopause height (TP_z) is defined by the lapse-rate tropopause (LR TP) *World Meteorological Organization* [1957] criterion, unless stated otherwise. The near-TP synoptic situation is obtained from ERA-Interim reanalysis [*Dee et al.*, 2011]. The 200 hPa level was selected for comparison with earlier work about the TIL relationship with relative vorticity [*Randel et al.*, 2007; *Randel and Wu*, 2010]. Daily, 12 UTC fields of geopotential height and winds are retrieved from ERA-Interim on a $2.5° \times 2.5°$ longitude-latitude grid. Relative vorticity and its curl and shear terms are calculated from the wind fields. Our study was conducted for the time period 2007–2013.

2.1. TIL Strength and Mapping

Static-stability vertical profiles are obtained from the COSMIC temperature data, calculating the Brunt-Väisälä frequency squared (N^2 [s^{-2}]) with the following formula:

$$N^2 = g/\Theta \cdot \partial\Theta/\partial z$$

where g is the gravitational acceleration and Θ the potential temperature. As a measure of TIL strength, we use the maximum of the Brunt-Väisälä frequency squared (N^2_{max}) above the LR TP, following *Birner et al.* [2006], *Wirth and Szabo* [2007], and *Erler and Wirth* [2011].

N^2_{max} represents TP sharpness better than the temperature difference between TP_z and 2 km above used in *Randel et al.* [2007] and *Randel and Wu* [2010] in terms of physical meaning: it captures the maximum gradient of potential temperature, and N^2 is used in wave propagation/refraction indexes and wave theory approximations. Instead of averaging the N^2 profiles with respect to the tropopause, the simple mean of all their N^2_{max} is made directly for two reasons: (1) the N^2_{max} is not always located at the exact same distance from the tropopause and therefore gets diluted in the TP-based average profile; and (2) there exists a cyclone-anticyclone asymmetry between the LR TP (based on temperature gradient) and dynamical tropopause (based on a potential vorticity threshold) [*Wirth*, 2001], with increasing differences toward stronger cyclonic circulation. Taking the mean of N^2_{max} avoids these sources of indeterminacy. We allow our algorithm to find the N^2_{max} up to 3 km above the tropopause, although it is almost always found in the first 1–2 km.

TIL strength maps are displayed daily on a polar stereographic grid covering the area of 30°–90°N (41 × 41 grid points with ~3° spacing). All GPS-RO profiles of the corresponding day within a 1000 km radius from each grid point are used to obtain the grid's value. The 1000 km radius is chosen to minimize the number of gaps in our TIL strength maps and for smoothing purposes since it avoids small-scale structures that cannot be resolved with the COSMIC mission sampling density. These settings are well below the size of troughs/ridges that form within baroclinic waves at near-TP level in winter and therefore sufficient to follow their synoptic development.

2.2. Relative Vorticity and Split Into Curl and Shear

Relative vorticity (ζ) and its curl and shear terms are obtained by applying the notation developed in *Bell and Keyser* [1993] on ERA-Interim (daily 12 UTC 200 hPa) wind fields. $Curl_\zeta$ and $Shear_\zeta$ are calculated as follows:

$$Curl_\zeta = 1/V^2[u^2 v_x - v^2 u_y - uv(u_x - v_y)] \quad (1)$$

$$Shear_\zeta = -1/V^2[u^2 u_y - v^2 v_x - uv(u_x - v_y)] \quad (2)$$

where $V^2 = (u^2 + v^2)$ and the subscripts of u and v denote their partial derivatives with respect to x or y. This notation is very convenient since the sum of (1) and (2) gives $(v_x - u_y) = \zeta$.

The 200 hPa relative vorticity and geopotential height fields are interpolated from the original ERA-Interim longitude-latitude grid onto the polar stereographic projection used in our analysis. Examples of the spatial distribution of $Curl_\zeta$ and $Shear_\zeta$ compared to ζ are given in the supporting information (Figure S1).

When making diagrams of TIL strength versus relative vorticity, we follow the method by *Randel et al.* [2007] and *Randel and Wu* [2010], binning TIL properties regarding their collocated 200 hPa relative vorticity. We use 12 UTC daily ERA-Interim [*Dee et al.*, 2011] instead of daily National Centers for Environmental Prediction (NCEP) reanalysis fields [*Kalnay et al.*, 1996] and N^2_{max} as the measure of TIL strength instead of the temperature difference between the TP_z and 2 km above. For each value of ζ, a distribution of N^2_{max} from all GPS-RO profiles collocated with such relative vorticity is computed. The $Curl_\zeta$ and $Shear_\zeta$ terms are also binned for comparison. In each case ζ, $Curl_\zeta$ and $Shear_\zeta$ are binned alone, regardless of what value the other terms have.

3. Synoptic-Scale Behavior of the TIL From Daily Snapshots

The synoptic-scale behavior of the TIL strength (sTIL) is analyzed based on snapshots of different summer and winter days. To take near-TP synoptic variability into account, the examples chosen for this section are representative of a range of situations that can be found in summer and winter: stronger/weaker N^2_{max} peaks and

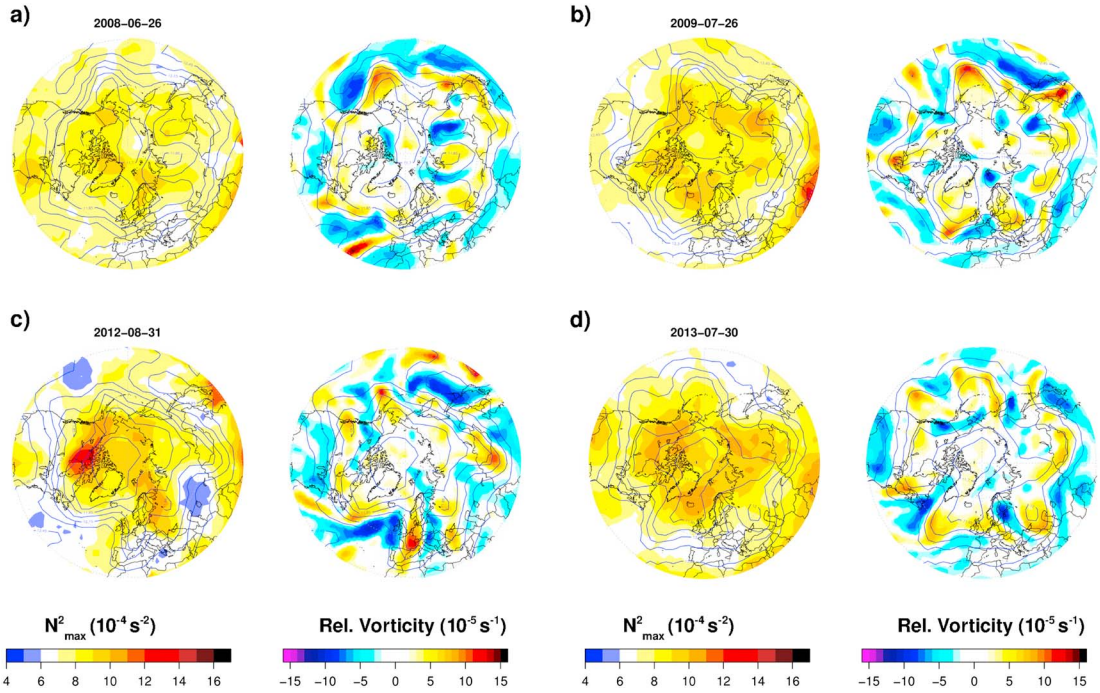

Figure 1. Polar stereographic maps of (first and third columns) daily TIL strength (N^2_{max}) and (second and fourth columns) 200 hPa relative vorticity, at different summer days. Corresponding color scales are at the bottom. Contour lines show 200 hPa geopotential height (in km with 150 m interval).

the presence of various zonal structures such as troughs and ridges of different wavelenghts and amplitudes. The results of this section are compared to earlier observational studies and climatologies [*Birner*, 2006; *Randel et al.*, 2007; *Randel and Wu*, 2010; *Grise et al.*, 2010], unless referred otherwise.

3.1. Summer Examples

Figure 1 shows four examples of sTIL daily snapshots during summer and the corresponding near-tropopause (12 UTC, 200 hPa) ζ and geopotential height fields of the same day. Note that due to our definition of sTIL via N^2_{max}, the magnitude of the sTIL is higher than in previous studies [*Birner*, 2006; *Randel et al.*, 2007; *Randel and Wu*, 2010; *Grise et al.*, 2010], differing about $2 \times 10^{-4}s^{-2}$.

In summer, the polar TIL is stronger than in midlatitudes. *Randel and Wu* [2010] showed that water vapor radiative effects dominate TIL formation in polar summer, since the highest upper tropospheric concentrations and cross-TP gradients are found then. The daily snapshots in Figure 1 reveal that the sTIL has high zonal and day-to-day variability, showing sTIL maxima collocated with anticyclonic relative vorticity. This is also in agreement with *Randel and Wu* [2010] who suggested that synoptic-scale dynamics shape the horizontal structure of the already strong polar summer TIL.

sTIL ranges typically between $8–10 \times 10^{-4}s^{-2}$ at polar regions and $6–7 \times 10^{-4}s^{-2}$ at midlatitudes. This is far away from typical stratospheric values ($\sim 4 \times 10^{-4}s^{-2}$) and supports the TIL as an absolutely ubiquitous feature in Northern Hemisphere (NH) summer. The weakest TIL found in some cases (Figure 1c, blue) has still values above $5 \times 10^{-4}s^{-2}$. In rare cases, the sTIL reaches more than $11 \times 10^{-4}s^{-2}$ (Figure 1c, red). Such events happen once per month on average and last 1–2 days.

3.2. Winter Examples

Figure 2 shows more sTIL snapshots from winter to compare with Figure 1 (summer). The geopotential height fields now show a stronger jet with larger-amplitude oscillations: well-defined troughs and ridges at midlatitudes. Due to the enhanced dynamic activity in midlatitude winters, we separated example days where the sTIL had very strong peaks (Figures 2a, 2c, 2e, and 2g) from days when it was weaker (Figures 2b, 2d, 2f, and 2h). The magnitude of N^2_{max} suggests that the TIL in NH winter is always present. Values below $5 \times 10^{-4}s^{-2}$ are only found in SH winter in the polar vortex region (see supporting information Figure S3).

In winter midlatitudes, the TIL is, in general, stronger than near the pole in agreement with previous climatologies [*Birner*, 2006; *Randel et al.*, 2007; *Randel and Wu*, 2010; *Grise et al.*, 2010] due to the increased

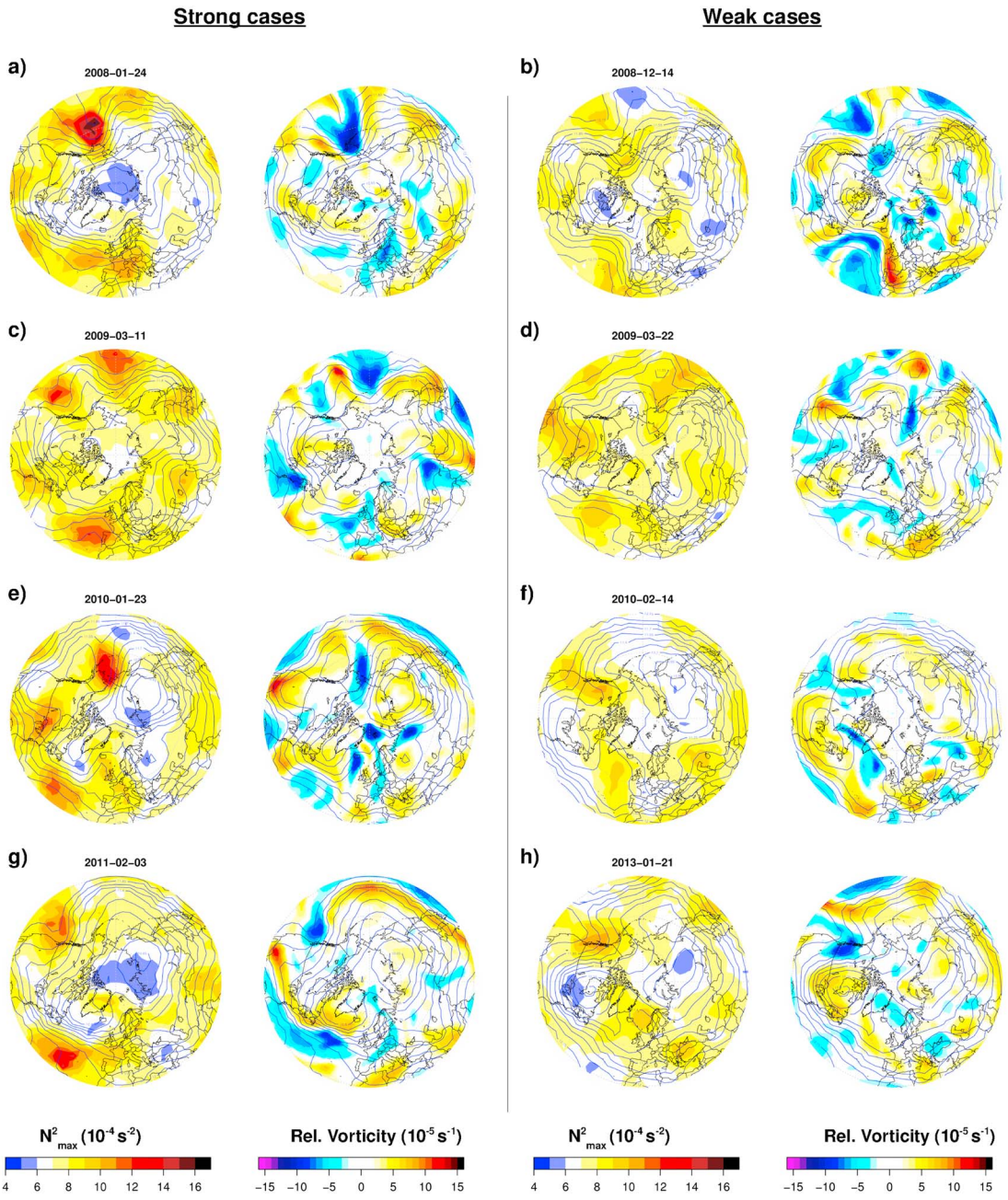

Figure 2. Same as Figure 1, but for different winter days. Separated are examples of situations with (a, c, e, and g) stronger N^2_{max} peaks and (b, d, f, and h) weaker N^2_{max} peaks.

stratospheric circulation in the winter hemisphere and upper tropospheric baroclinic wave activity at midlatitudes. The TIL adjusts to the synoptic circulation, showing a big trough-ridge contrast. Lower values of $6–7 \times 10^{-4}s^{-2}$ are found within troughs and peaks of at least $8–10 \times 10^{-4}s^{-2}$ within ridges (Figures 2b, 2d, 2f, and 2h), while the sTIL at polar regions is about $5–7 \times 10^{-4}s^{-2}$. The sTIL quite often reaches more than $12 \times 10^{-4}s^{-2}$ within midlatitude ridges, and depending on the wave structure of the jet, one (Figure 2a) or multiple strong peaks (Figures 2c, 2e, and 2g) can appear. As in summer, those strong peaks last for 1–2 days but are present more often: about 25% of all days. The trough-ridge contrast from Figure 2 is coherent with the TIL zonal structures derived from reanalysis by *Gettelman and Wang* [2015].

Why is the TIL within ridges in midlatitude winter of the same magnitude or stronger than in polar summer? During winter the stratospheric residual circulation is strongest (producing dynamical heating above the TP),

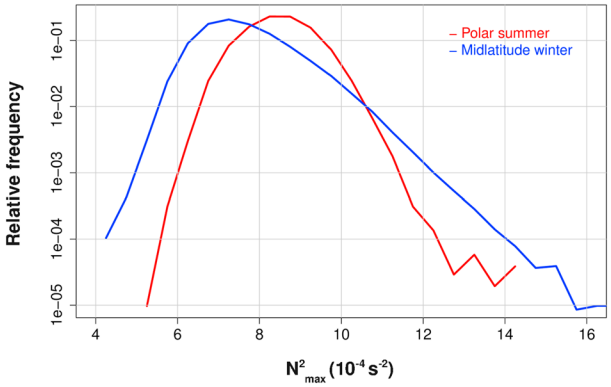

Figure 3. Histogram with relative frequencies of TIL strength (N^2_{max}), comparing Northern Hemisphere polar summer (red line, JJAS 70°–90°N) with midlatitude winter (blue line, DJFM 30°–60°N).

tropopause lifting and cooling by upper-tropospheric eddies are strongest at midlatitudes (and especially within ridges since they have higher and colder TP), and even radiative cooling from cirrus clouds or high humidity at near-TP level is possible. *Taylor et al.* [2011] showed a case study of a nonconvective cirrus cloud associated with a negative temperature anomaly, and *Biondi et al.* [2012] studied the temperature inversion generally found at cloud tops with GPS-RO data.

While all three mechanisms can act together in ridges, this is not the case in troughs (lower TP, no high cirrus clouds) or polar summer (upper tropospheric eddies and stratospheric circulation are both weaker despite the stronger water vapor radiative cooling).

3.3. Polar Summer Versus Midlatitude Winter

Figure 3 summarizes the results from sections 3.1 and 3.2, showing the relative frequency of N^2_{max} in polar summer (red line) and midlatitude winter (blue line). The N^2_{max} occurrence is computed relative to all grid boxes (from maps as in Figures 1 and 2) within the selected latitudes and time. The seasonal mean state of the sTIL in polar summer ($8.5 \times 10^{-4}s^{-2}$) is stronger than in midlatitude winter ($7.6 \times 10^{-4}s^{-2}$). Note that the distributions are shown on a log-*y* scale, and due to the large sample size (2007–2013, daily for each season, multiple grid points, less area/grids in polar regions), this difference is very significant: 100 standard deviations of the distributions' means are $0.25 \times 10^{-4}s^{-2}$ for summer and $0.12 \times 10^{-4}s^{-2}$ for winter.

The midlatitude winter distribution (though having a lower mean) is much broader and skewed toward higher N^2_{max} values, which only occur within ridges as shown in the previous section. sTIL values surpassing the summer mean ($8.5 \times 10^{-4}s^{-2}$) represent an integrated relative frequency of 19.14% in the midlatitude winter distribution. Values above $10 \times 10^{-4}s^{-2}$ amount for a 3.24%, and the strongest peaks above $11 \times 10^{-4}s^{-2}$ are more frequent in midlatitude winter than in polar summer.

In summary, the synoptic-scale features shown in this section reveal that the strongest TIL is found in midlatitude winter, within ridges. Even in the weakest cases, the sTIL within midlatitude ridges in winter (Figure 2) is of the same magnitude ($8–10\times10^{-4}s^{-2}$) as in polar summer (Figure 1), and the strongest sTIL peaks are more frequent and reach higher values within winter ridges compared to polar summer (Figure 3). Due to the big trough-ridge contrast (weak-strong TIL), the zonal mean sTIL in midlatitude winter is weaker than in polar summer (Figure 3), in agreement with earlier climatologies [*Birner*, 2006; *Randel et al.*, 2007; *Randel and Wu*, 2010; *Grise et al.*, 2010].

All results from this section are also applicable to the Southern Hemisphere extratropical TIL. Plots similar to Figures 1–3 can be found in the supporting information (Figures S2–S4).

4. The Role of Curl and Shear Relative Vorticity

Figures 4a and 4b show diagrams of TIL strength (N^2_{max}) related to relative vorticity for polar summer and midlatitude winter, respectively. Thick lines show the mean N^2_{max} for each relative vorticity bin, while the vertical thin lines show one standard deviation of the bin's N^2_{max} distribution's mean. The black lines (total relative vorticity) in Figure 4b correspond to the results from *Randel et al.* [2007] and those in Figure 4a to the ones from *Randel and Wu* [2010]. Even using different reanalysis data and a different measure for the sTIL, its relationship with ζ is in very good agreement with those earlier studies: sTIL increases toward anticyclonic conditions in a very similar manner. Due to the larger sample size, high measure density by COSMIC mission [*Anthes et al.*, 2008] and a longer time period (2007–2013), a wider range of ζ can be explored.

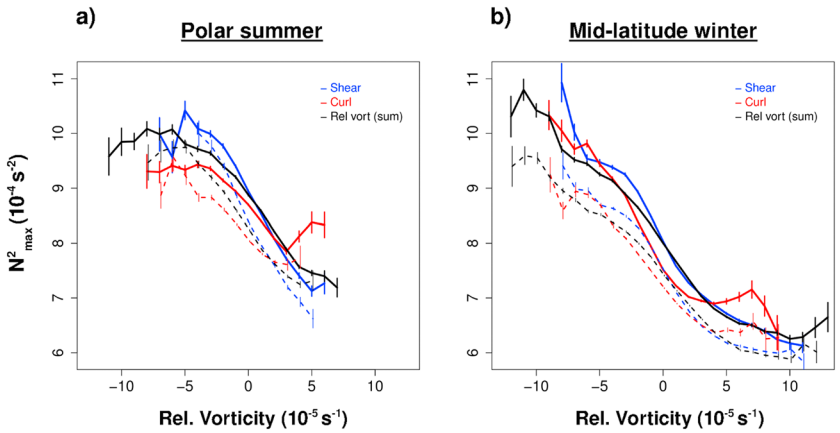

Figure 4. Diagrams of TIL strength (N^2_{max}) versus relative vorticity. (a) Polar summer (JAS 70°–90°N) and (b) midlatitude winter (JFM 30°–60°N). Blue, red, and black lines denote, respectively, shear, curl, and total relative vorticity. Dashed lines correspond to Southern Hemisphere seasons (summer JFM and winter JAS). Vertical bars denote one standard deviation of the mean value.

4.1. Curl in Cyclonic Circulation

The red and blue lines in Figure 4 correspond to the $Curl_\zeta$ and $Shear_\zeta$ terms. Figure 4 shows that the general tendency of decreasing sTIL with stronger cyclonic circulation is not followed by the $Curl_\zeta$ term (red line): the relation gets inverted at the strongest cyclonic $Curl_\zeta$ with values showing enhanced sTIL.

Nonlinear growth and breaking of baroclinic waves can generate high $Curl_\zeta$ amounts [*Bell and Keyser*, 1993], and the behavior of the $Curl_\zeta$ line in Figure 4 is particularly similar to the N^2_{max} versus relative vorticity relation described by *Erler and Wirth* [2011] after the anticyclonic breaking (LC1 type) of a baroclinic wave. Our results suggest that processes related to baroclinic wave growth and breaking (e.g., flow imbalance or gravity wave presence) [*Plougonven and Zhang*, 2014; *Kunkel et al.*, 2014] are responsible for the enhancement of the weaker TIL within cyclones.

4.2. Shear in Anticyclonic Circulation

$Curl_\zeta$ (red) and $Shear_\zeta$ (blue) terms in Figure 4 differ increasingly toward stronger anticyclonic conditions. Strong anticyclonic $Shear_\zeta$ is related to higher values of N^2_{max}. The difference of the mean sTIL at the same values of $Curl_\zeta$ and $Shear_\zeta$ is significant in Figure 4a: the blue and red lines are separated by more than one standard deviation (vertical lines). For midlatitude winter sTIL (Figure 4b) the lines differ less, though having the same tendency. The same behavior is observed regarding TP_z, with anticyclonic shear related to the highest TP_z (see supporting information Figure S5) and differing significantly from the $Curl_\zeta$ term at any season. Polar winter has a similar behavior as in Figure 4a, and midlatitude summer resembles Figure 4b (see supporting information Figure S6).

Wirth [2003] explained the stronger TIL in anticyclones by hydrostatic and gradient wind balance. Since the wind shear dominates this balance, our results for the shear term further support these dynamics in producing the strong TIL within anticyclonic conditions. *Wirth* [2004] showed that the same dynamics, apart from making the tropopause higher and colder in the anticyclone, also form a secondary circulation with downwelling and convergence of vertical wind above the anticyclone, bringing the isentropes closer, increasing the potential temperature gradient and thus further stabilizing the TIL region.

As in section 3, the results of this section also apply to the Southern Hemisphere. The roles of the $Curl_\zeta$ and $Shear_\zeta$ terms are very similar (dashed lines in Figure 4, and supporting information Figures S5 and S6).

5. Concluding Remarks

Our study analyzed the TIL real-time behavior, showing important features adjusted to the synoptic situation at near-tropopause level, especially a strong trough-ridge contrast in midlatitude winter. The key finding of our study is that the TIL within midlatitude winter ridges is always as strong or even stronger than

in polar summer. This means that while the climatological TIL is strongest in polar summer [*Birner*, 2006; *Randel et al.*, 2007; *Randel and Wu*, 2010; *Grise et al.*, 2010], this is no longer the case at the synoptic scale. This highlights the importance of synoptic-scale dynamics for the formation of the TIL.

We expanded the work by *Randel et al.* [2007] and *Randel and Wu* [2010] on the relationship of sTIL with relative vorticity. Shear relative vorticity is related to the strongest TIL in anticyclonic conditions, especially at polar latitudes, while the weaker TIL within cyclones is enhanced under the Curl_ζ term. This suggests that the processes responsible for the TIL enhancement are different in anticyclones (balanced hydrostatic dynamics) and cyclones (related to baroclinic wave growth and breaking).

All these findings also apply for the Southern Hemisphere. We are aware that the 200 hPa level chosen as the near-tropopause synoptic situation is often quite above the tropopause and more representative of the lowermost stratosphere: there is high variability in TP_z at midlatitudes, and TP_z at polar regions is typically below 250 hPa even in summer [*Son et al.*, 2011]. Nevertheless, it is very useful for comparison with earlier studies about the TIL.

Acknowledgments
This study was completed within the Helmholtz University Young Investigators Group NATHAN project, funded by the Helmholtz Association through the president's Initiative and Networking Fund and the GEOMAR, Helmholtz Centre for Ocean Research Kiel. We thank the ECMWF data server for the free availability of ERA-Interim data and UCAR for the COSMIC satellite mission temperature profiles. We are grateful to two anonymous reviewers for their valuable comments. We also appreciate the assistance accessing different data sets and discussions in the early stages of this study by Wuke Wang and Sebastian Wahl.

References

Anthes, R. A., et al. (2008), The COSMIC/FORMOSAT-3 mission: Early results, *Bull. Am. Meteorol. Soc.*, *89*, 313–333, doi:10.1175/BAMS-89-3-313.

Bell, G. D., and D. Keyser (1993), Shear and curvature vorticity and potential-vorticity interchanges: Interpretation and application to a cutoff cyclone event, *Mon. Weather Rev.*, *121*, 76–102, doi:10.1175/1520-0493(1993)121<0076:SACVAP>2.0.CO;2.

Biondi, R., W. J. Randel, S.-P. Ho, T. Neubert, and S. Syndergaard (2012), Thermal structure of intense convective clouds derived from GPS radio occultations, *Atmos. Chem. Phys.*, *12*, 5309–5318, doi:10.5194/acp-12-5309-2012.

Birner, T. (2006), Fine-scale structure of the extratropical tropopause region, *J. Geophys. Res.*, *111*, D04104, doi:10.1029/2005JD006301.

Birner, T. (2010), Residual circulation and tropopause structure, *J. Atmos. Sci.*, *67*, 2582–2600, doi:10.1175/2010JAS3287.1.

Birner, T., A. Dörnbrack, and U. Schumann (2002), How sharp is the tropopause at midlatitudes?, *Geophys. Res. Lett.*, *29*, 1700, doi:10.1029/2002GL015142.

Birner, T., D. Sankey, and T. G. Shepherd (2006), The tropopause inversion layer in models and analyses, *Geophys. Res. Lett.*, *33*, L14804, doi:10.1029/2006GL026549.

Das, U., and C. J. Pan (2014), Validation of FORMOSAT-3/COSMIC level 2 "atmPrf" global temperature data in the stratosphere, *Atmos. Meas. Tech.*, *7*, 731–742, doi:10.5194/amt-7-731-2014.

Dee, D. P., et al. (2011), The ERA-Interim reanalysis: Configuration and performance of the data assimilation system, *Q. J. R. Meteorol. Soc.*, *137*, 553–597, doi:10.1002/qj.828.

Erler, A. R., and V. Wirth (2011), The static stability of the tropopause region in adiabatic baroclinic life cycle experiments, *J. Atmos. Sci.*, *68*, 1178–1193, doi:10.1175/2010JAS3694.1.

Gettelman, A., and T. Wang (2015), Structural diagnostics of the tropopause inversion layer and its evolution, *J. Geophys. Res. Atmos.*, *120*, 46–62, doi:10.1002/2014JD021846.

Grise, K. M., D. W. J. Thompson, and T. Birner (2010), A global survey of static stability in the stratosphere and upper troposphere, *J. Clim.*, *23*, 2275–2292, doi:10.1175/2009JCLI3369.1.

Hegglin, M. I., C. D. Boone, G. L. Manney, and K. A. Walker (2009), A global view of the extratropical tropopause transition layer from Atmospheric Chemistry Experiment Fourier Transform Spectrometer O_3, H_2O, and CO, *J. Geophys. Res.*, *114*, D00B11, doi:10.1029/2008JD009984.

Kalnay, E., et al. (1996), The NCEP/NCAR 40-Year Reanalysis Project, *Bull. Am. Meteorol. Soc.*, *77*, 437–472, doi:10.1175/1520-0477(1996)077<0437:TNYRP>2.0.CO;2.

Kunkel, D., P. Hoor, and V. Wirth (2014), Can inertia-gravity waves persistently alter the tropopause inversion layer?, *Geophys. Res. Lett.*, *41*, 7822–7829, doi:10.1002/2014GL061970.

Kunz, A., P. Konopka, R. Müller, L. L. Pan, C. Schiller, and F. Rohrer (2009), High static stability in the mixing layer above the extratropical tropopause, *J. Geophys. Res.*, *114*, D16305, doi:10.1029/2009JD011840.

Miyazaki, K., S. Watanabe, Y. Kawatani, Y. Tomikawa, M. Takahashi, and K. Sato (2010a), Transport and mixing in the extratropical tropopause region in a high-vertical-resolution GCM. Part I: Potential vorticity and heat budget analysis, *J. Atmos. Sci.*, *67*, 1293–1314, doi:10.1175/2009JAS3221.1.

Miyazaki, K., S. Watanabe, Y. Kawatani, K. Sato, Y. Tomikawa, and M. Takahashi (2010b), Transport and mixing in the extratropical tropopause region in a high-vertical-resolution GCM. Part II: Relative importance of large-scale and small-scale dynamics, *J. Atmos. Sci.*, *67*, 1315–1336, doi:10.1175/2009JAS3334.1.

Plougonven, R., and F. Zhang (2014), Internal gravity waves from atmospheric jets and fronts, *Rev. Geophys.*, *52*, 33–76, doi:10.1002/2012RG000419.

Randel, W. J., and F. Wu (2010), The polar summer tropopause inversion layer, *J. Atmos. Sci.*, *67*, 2572–2581, doi:10.1175/2010JAS3430.1.

Randel, W. J., F. Wu, and P. Forster (2007), The extratropical tropopause inversion layer: Global observations with GPS data, and a radiative forcing mechanism, *J. Atmos. Sci.*, *64*, 4489–4496, doi:10.1175/2007JAS2412.1.

Schmidt, T., J.-P. Cammas, H. G. J. Smit, S. Heise, J. Wickert, and A. Haser (2010), Observational characteristics of the tropopause inversion layer derived from CHAMP/GRACE radio occultations and MOZAIC aircraft data, *J. Geophys. Res.*, *115*, D24304, doi:10.1029/2010JD014284.

Son, S.-W., and L. M. Polvani (2007), Dynamical formation of an extra-tropical tropopause inversion layer in a relatively simple general circulation model, *Geophys. Res. Lett.*, *34*, L17806, doi:10.1029/2007GL030564.

Son, S.-W., N. F. Tandon, and L. M. Polvani (2011), The fine-scale structure of the global tropopause derived from COSMIC GPS radio occultation measurements, *J. Geophys. Res.*, *116*, D20113, doi:10.1029/2011JD016030.

Taylor, J. R., W. J. Randel, and E. J. Jensen (2011), Cirrus cloud-temperature interactions in the tropical tropopause layer: A case study, *Atmos. Chem. Phys.*, *11*, 10,085–10,095, doi:10.5194/acp-11-10085-2011.

Wirth, V. (2001), Cyclone-anticyclone asymmetry concerning the height of the thermal and the dynamical tropopause, *J. Atmos. Sci.*, *58*, 26–37, doi:10.1175/1520-0469(2001)058<0026:CAACTH>2.0.CO;2.
Wirth, V. (2003), Static stability in the extratropical tropopause region, *J. Atmos. Sci.*, *60*, 1395–1409, doi:10.1175/1520-0469(2003)060<1395:SSITET>2.0.CO;2.
Wirth, V. (2004), A dynamical mechanism for tropopause sharpening, *Meteorol. Z.*, *13*, 477–484, doi:10.1127/0941-2948/2004/0013-0477.
Wirth, V., and T. Szabo (2007), Sharpness of the extratropical tropopause in baroclinic life cycle experiments, *Geophys. Res. Lett.*, *34*, L02809, doi:10.1029/2006GL028369.
World Meteorological Organization (1957), Meteorology—A three-dimensional science, *WMO Bull.*, *6*, 134–138.